

Clickable X-ray Nanoprobes for Nanoscopic Bioimaging of Cellular Structures

Qiaowei Tang,[‡] Dapeng Yin,[‡] Yubo Liu,[‡] Jichao Zhang, Yong Guan, Huating Kong, Yiliu Wang, Xiangzhi Zhang, Jiang Li, Lihua Wang, Jun Hu,* Xiaoqing Cai,* and Ying Zhu*



Cite This: *JACS Au* 2024, 4, 893–902



Read Online

ACCESS |

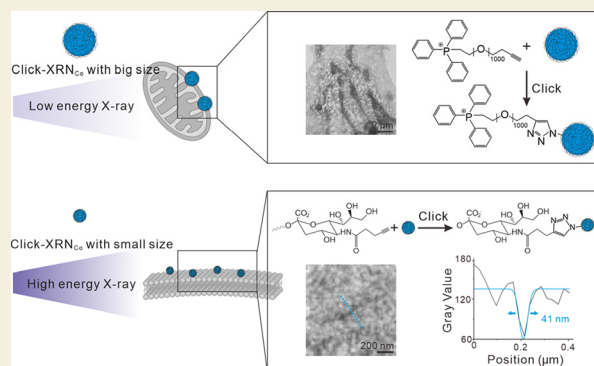
Metrics & More

Article Recommendations

Supporting Information

ABSTRACT: Synchrotron-based X-ray microscopy (XRM) has garnered widespread attention from researchers due to its high spatial resolution and excellent energy (element) resolution. Existing molecular probes suitable for XRM include immune probes and genetic labeling probes, enabling the precise imaging of various biological targets within cells. However, immune labeling techniques are prone to cross-interference between antigens and antibodies. Genetic labeling technologies have limited systems that allow express markers independently, and moreover, genetically encoded labels based on catalytic polymerization lack a fixed morphology. When applied to cell imaging, this can result in reduced localization accuracy due to the diffusion of labels within the cells. Therefore, both techniques face challenges in simultaneously labeling multiple biotargets within cells and achieving high-precision imaging. In this work, we applied the click reaction and developed a third category of imaging probes suitable for XRM, termed clickable X-ray nanoprobes (Click-XRN). Click-XRN consists of two components: an X-ray-sensitive multicolor imaging module and a particle-size-controllable morphology module. Efficient identification of intra- and extracellular biotargets is achieved through click reactions between the probe and biomolecules. Click-XRN possesses a controllable particle size, and its loading of various metal ions provides distinctive signals for imaging under XRM. Based on this, we optimized the imaging energy of Click-XRN with different particle sizes, enabling single-color and two-color imaging of the cell membrane, cell nucleus, and mitochondria with nanoscale spatial nanometers. Our work provides a potent molecular tool for investigating cellular activities through XRM.

KEYWORDS: *clickable X-ray nanoprobes, synchrotron-based nanoscopic imaging, cellular structure, polydopamine nanoparticle, metal ion*



INTRODUCTION

One of the fundamental goals of cell biology is to understand the complex spatiotemporal interactions of biomolecules in their natural cellular environment.^{1,2} Owing to the X-ray wavelength falls within the range of 0.1–10 nm, Synchrotron-based X-ray microscopy (XRM) is a super-resolution microscopic imaging technology with a theoretical resolution of several nanometers.^{3–8} Compared to electron beams, X-rays exhibit enhanced penetration capabilities toward biological samples, enabling the imaging of intact cells without sectioning.^{9,10} Moreover, X-rays can capture the inherent contrast of cells within the “water window” (wavelength 2.4–4.4 nm) band.^{11–13} Notably, X-rays offer excellent energy (elemental) resolution. Exploiting differences in X-ray fluorescence (XRF) emission spectra from different elements enables the development of multicolor labels.^{14–17} This approach can be employed for the development of biological probes to achieve the recognition and imaging of diverse biomolecules within cells.

Currently, two primary categories of probes suitable for XRM have been developed: immune probes and genetic probes. Immune probes primarily employ TiO₂, quantum dots, and other nanoparticles possessing X-ray absorption characteristics in conjunction with the antigen–antibody reaction to achieve the labeling of intracellular biological targets. These probes rely on specific binding interactions between antigens and antibodies, and identical or similar structural determinants often result in crosstalk among different antigens.^{18–22} Utilizing engineered peroxidases as genetically encoded X-ray-sensitive tags, the genetic probes catalyze the polymerization of X-ray-sensitive substrates to form X-ray-visible polymers. However, there is a scarcity of existing systems

Received: January 18, 2024

Revised: February 5, 2024

Accepted: February 7, 2024

Published: March 11, 2024



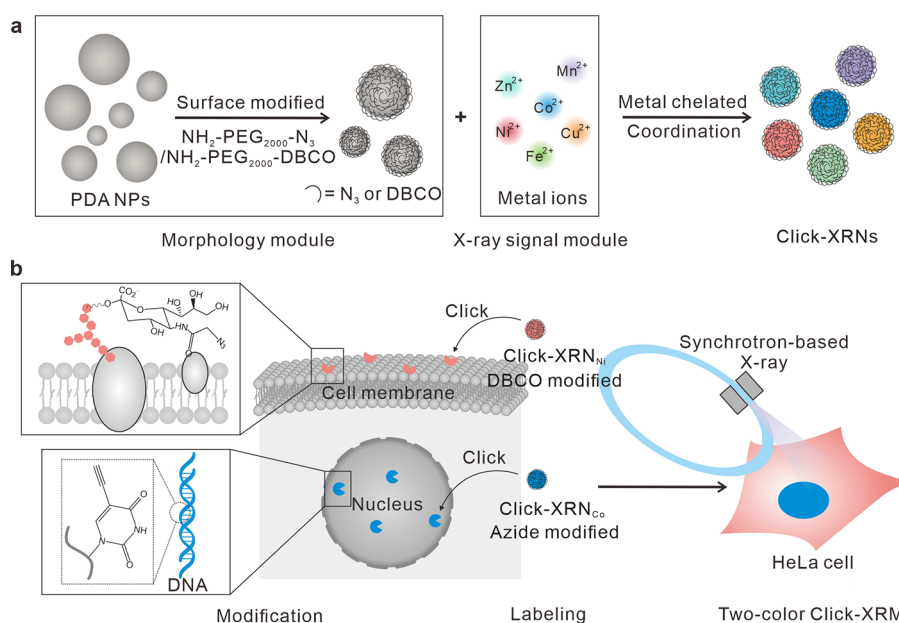


Figure 1. Design of Click-XRNs and clickable X-ray microscopy (Click-XRM). (a) Click-XRNs (right) consist of two modules: (1) surface-modified PDA NPs as the morphology module (left) with controllable particle size and (2) various metal ions as the X-ray signal module (middle). (b) Schematic diagram of two-color Click-XRM. The cell membrane and nucleus of HeLa cells were modified with the necessary groups for the click reaction, followed by sequential labeling using Click-XRN_{Ni} (DBCO modified) and Click-XRN_{Co} (azide modified), and imaging under XRM.

capable of independently staged expression, with only the photocatalytic mini-Singlet Oxygen Generator (MiniSOG) and the non-photo-catalytic ascorbate peroxidase APEX2 being available.²³ Additionally, the polymer utilized by the genetic probes to generate X-ray signals exhibits no fixed morphology, thereby compromising the precision of cellular imaging due to label diffusion within cells, which is an inherent limitation of this type of imaging probes. Therefore, achieving simultaneous high-precision imaging of multiple biological target molecules in cellular activities using the two types of synchrotron-based X-ray probes described above is challenging.

Inspired by the widely employed concept of click chemistry,^{24–28} we developed a third class of imaging probes suitable for XRM, called clickable X-ray nanoprobess (Click-XRN). We synthesized polydopamine nanoparticles (PDA NPs) with varying particle sizes and surface-modified them with functional groups (azide or dibenzo cyclooctyne (DBCO) groups) for subsequent click reactions. PDA NPs can chelate various metal ions, thereby enabling distinct X-ray imaging signals (Figure 1a). We systematically assessed the chelation capacity of PDA NPs for metal ions and the stability and cytotoxicity of the Click-XRNs. Furthermore, we screened the particle size of this probe and the imaging energy of X-rays for different biological targets. On this basis, we successfully achieved recognition and imaging of various biotargets within cells (Figure 1b). Finally, combined with the excellent energy resolution of synchrotron-based X-ray, we successfully achieved multicolor imaging of two biotargets within cells.

RESULTS

Design, Synthesis, and Characterization of Click-XRNs

First, we describe the design and characterization of Click-XRNs. The design of our study is illustrated in Figure 1a, where Click-XRNs consist of two modules: (1) morphology module with controllable particle size and (2) X-ray-sensitive imaging module. The first module comprises surface-modified

PDA NPs, wherein the PDA NPs are obtained through a reaction mixture of dopamine hydrochloride, ammonia, and ethanol. The particle size of PDA NPs is controlled by adjusting the ratio between dopamine hydrochloride and ammonia to ensure a fixed size for PDA NPs as the cores in Click-XRNs. The second module comprises various metal ions. Synchrotron-based X-rays offer excellent energy (element) resolution, with narrow and distinguishable XRF signal peaks for different metal elements. Therefore, they can provide Click-XRN with distinctive X-ray imaging signals. The coordination between metal ions in X-ray signal module and catechol or carboxyl groups in morphology module can be achieved without the need for external chelating agents.²⁹

To meet the labeling and imaging requirements of diverse biological targets, we synthesized PDA NPs with varying sizes (Figure 2a). The synthesis involved incorporating dopamine hydrochloride into a mixed aqueous solution of ammonia and ethanol while adjusting the ratio between ammonia and dopamine hydrochloride to modulate the particle size. Transmission electron microscopy (TEM) imaging and dynamic light scattering (DLS) statistical analysis showed that different amounts of ammonia–water (0.4 mL, 0.6 mL, 1 mL, 1.5 mL, and 2 mL) resulted in average particle sizes of PDA NPs measuring at 841.7, 374.6, 244.9, 154.7, and 111.6 nm, respectively (Figure 2b), indicating a negative correlation between ammonia content in the reaction system and the size of PDA NPs (Figure 2b). Furthermore, PDA NPs with an average size of 111.6 nm were sonicated, and the retentate was collected using a centrifugal filter (MWCO = 30 kDa). TEM imaging revealed that small-PDA NPs (sPDA NPs) with an average size of 3.7 nm could be obtained (Figure 2c). The surface potentials of 841.7, 374.6, 244.9, 154.7, 111.6, and 3.7 nm sized PDA NPs were determined to be –40.0 mV, –40.1 mV, –44.0 mV, –33.6 mV, –36.3 mV, and –28.5 mV, respectively. PDA NPs were dispersed in physiological environments including Mill-Q water, normal saline, and

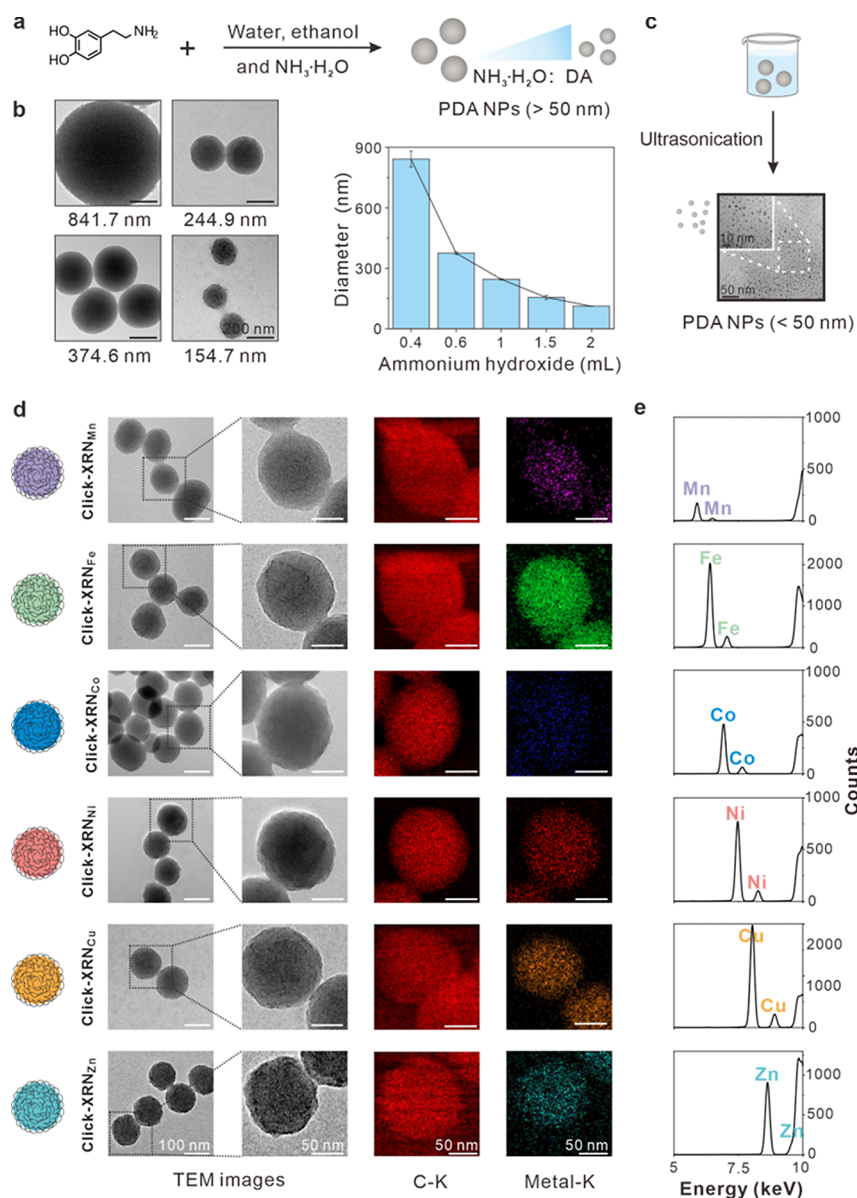


Figure 2. Preparation and characterization of Click-XRNs. (a) Synthesis of PDA NPs. Dopamine hydrochloride was incorporated into a mixed aqueous solution of ammonia and ethanol to obtain PDA NPs and the particle size of PDA NPs was modulated by adjusting the ratio between ammonia and dopamine hydrochloride. b, TEM images of four types of PDA NPs with different particle sizes and corresponding diagram between the particle size of PDA NPs and the amount of ammonia–water used. The particle size of PDA NPs was inversely correlated with the amount of ammonia in the reaction system. (c) Synthesis and TEM images of sPDA NPs. PDA NPs with an average size of 111.6 nm were sonicated and the retentate was collected to obtain sPDA NPs. (d) EDS mapping of six Click-XRNs: TEM images of six Click-XRNs (first column), local magnification (second column), under the carbon absorption edge (third column), and under different metal edges (fourth column). Metal elements were uniformly enriched within the area of carbon element distribution. (e) XRF full spectra of six Click-XRNs. Distinct characteristic peaks corresponding to each metal element were observed in the spectra.

PBS. No sedimentation was observed after storage for 15 days (Figure S1), indicating their high stability under physiological conditions.

Next, using PDA NPs with an average size of 111.6 nm as a representative, we prepared metal-containing Click-XRNs. We adjusted the pH of the reaction system to 9 and introduced azide-PEG-amine for surface azide modification of PDA NPs.³⁰ The DLS analysis revealed that the azide modification resulted in an increase in the average particle size of PDA NPs from 111.6 to 116.2 nm and the zeta potential from -36.3 to -34.4 mV (named as PDA- N_3). Then, we adjusted the pH of the PDA- N_3 solution to 5.5 using hydrochloric acid, followed by

addition of varying quantities of Mn^{2+} , Fe^{2+} , Co^{2+} , Ni^{2+} , Cu^{2+} , and Zn^{2+} solutions, resulting in mass ratios of metal ions to PDA- N_3 at 0.01, 0.05, 0.1, 0.2, 0.5, and 1, respectively. Finally, the mixed solutions were agitated for 3 h, and residual free metal ions were eliminated through rinse followed by centrifugation. Inductively coupled plasma-mass spectrometry (ICP-MS) analysis showed that at mass ratios of metal ions to PDA- N_3 are 0.01, 0.05, 0.1, 0.2, 0.5, and 1, Mn^{2+} in amounts of 28.8, 38.3, 43.5, 44.8, 44.2, and 44.7 μg , Fe^{2+} in amounts of 72.6, 111.4, 119.2, 133.7, 139.2, and 138.6 μg , Co^{2+} in amounts of 37.0, 44.6, 48.4, 57.7, 71.2, and 70.0 μg , Ni^{2+} in amounts of 39.8, 40.2, 49.1, 52.4, 51.6, and 52.3 μg , Cu^{2+} in amounts of

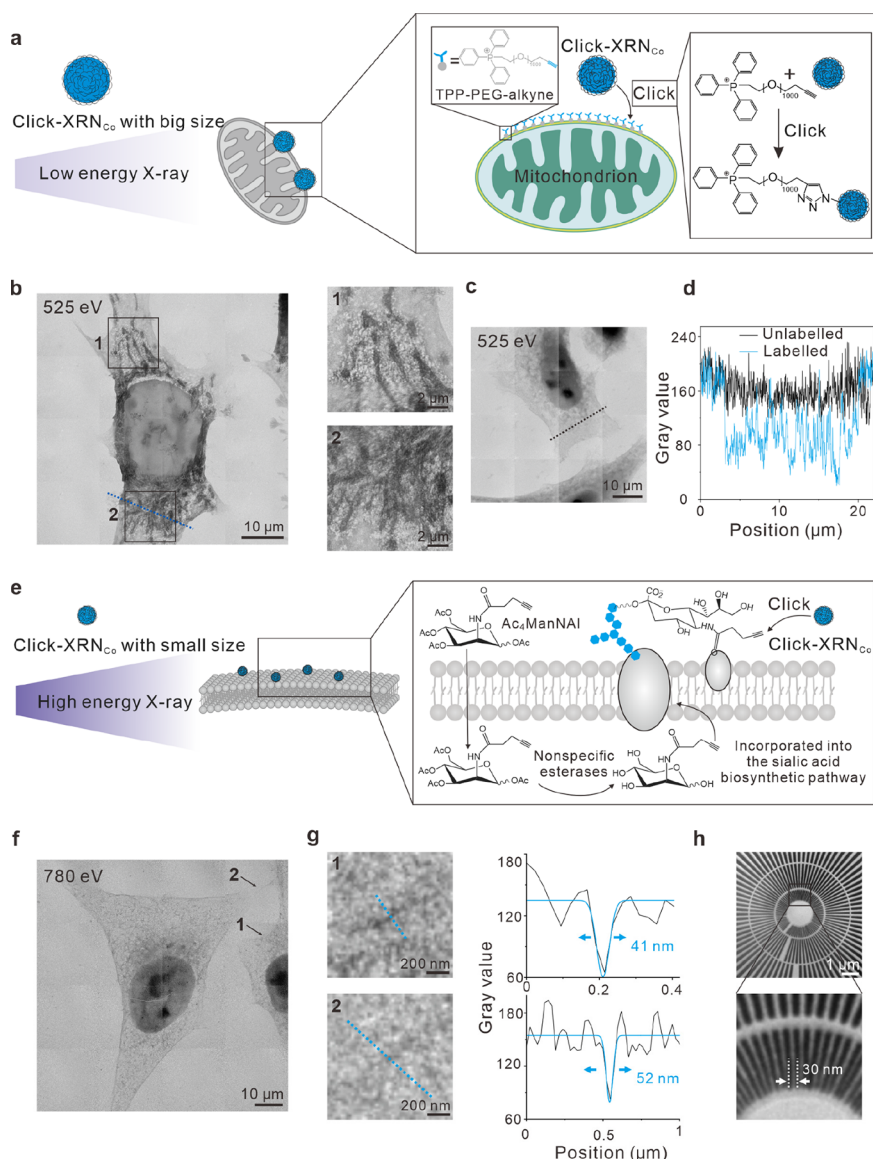


Figure 3. Versatility of Click-XRNs for labeling biological targets of different sizes. (a) The schematic diagram illustrating the use of Click-XRNs for labeling mitochondria. TPP-PEG-alkyne was incubated with the cells to modify alkyne groups on mitochondria. Click-XRN_{Co} (119.9 nm, azide-modified) was employed for mitochondrial recognition and labeling. (b) Image and local magnification of mitochondria in labeled cells at a photon energy of 525 eV. (c) Image of unlabeled cell at a photon energy of 525 eV. (d) The intensity profile of mitochondria outlines along dashed lines in (b) and (c). The gray image we collected has a bit depth of 8, with pixel values ranging from 0 to 255, representing a gradient of brightness from dark to light, and correspondingly, a range of colors from black to white. The intensity profiles were obtained by loading the gray value of the image using Fiji ImageJ. (e) The schematic diagram illustrating the use of Click-XRNs for labeling cell membrane. Ac₄ManNAI was incubated with the cells to modify alkyne groups on cell membrane. Click-XRN_{Co} (3.9 nm, azide-modified) was employed for cell membrane recognition and labeling. (f) Image of cell membrane in labeled cells at a photon energy of 780 eV. (g) Left: Magnification of the regions indicated by the arrows. Right: The intensity profile of cell membrane outlines along dashed lines. The intensity profiles were obtained by loading the gray value of the image using Fiji ImageJ. The structural features were inferred through 1D Gaussian fitting, and fwhm value was displayed on each profile. (h) X-ray imaging of test star-pattern sample. The inner circle demonstrated a spatial pattern of 30 nm.

70.3, 101.6, 120.1, 139.7, 142.3, and 142.8 μg , and Zn^{2+} in amounts of 57.7, 66.5, 84.7, 86.8, 88.4, and 87.9 μg were chelated by PDA-N₃ (1 mg, Figure S2a). This indicates that the loading of metal ions on PDA-N₃ does not increase with the increase in the feed ratio when the mass ratio of metal ions to PDA-N₃ reaches 0.5, which may be related to the limited coordination sites on the surface of PDA-N₃.

In subsequent experiments, we selected a metal ion to PDA-N₃ mass ratio of 0.5. Six different Click-XRNs were synthesized, each containing a distinct metal (named Click-XRN_{Mn}, Click-XRN_{Fe}, Click-XRN_{Co}, Click-XRN_{Ni}, Click-

XRN_{Cu}, and Click-XRN_{Zn}). We investigated the morphology and composition of different Click-XRNs by TEM-energy dispersive spectrometry (TEM-EDS) (Figure 2d). The TEM images revealed that the morphology of various types of Click-XRNs exhibited similarity and uniformity. We found that neither surface modification nor metal ion chelation had any significant impact on the morphology of PDA NPs (Figure 2d, left). After metal ion chelation, the particle sizes of Click-XRN_{Mn}, Click-XRN_{Fe}, Click-XRN_{Co}, Click-XRN_{Ni}, Click-XRN_{Cu}, and Click-XRN_{Zn} increased to 118.3, 120.4, 119.9, 121.0, 125.6, and 121.8 nm, respectively. The EDS energy

spectrum data demonstrated that distinct signal peaks corresponding to various metal elements could be observed in different types of Click-XRNs (Figure S3). Subsequently, EDS element mapping images illustrated the spatial distribution of C, Mn, Fe, Co, Ni, Cu, and Zn within different Click-XRNs (Figure 2d, middle, right). EDS mapping of carbon distribution was utilized to illustrate the distribution of Click-XRNs, as the dopamine hydrochloride comprises 8 carbon atoms. Additionally, metal elements were uniformly enriched within the area of the carbon element distribution, indicating uniform doping of diverse metal elements into different Click-XRNs. To evaluate the efficacy of the prepared probes in generating robust elemental signals under XRM, we conducted an analysis of synchrotron-based XRF for each probe. The K-absorption edges of Mn, Fe, Co, Ni, Cu, and Zn are 6.539, 7.112, 7.709, 8.333, 8.979, and 9.659 keV, respectively. K-absorption edge represents the minimum energy for excitation, while X-ray fluorescence denotes the emitted X-ray energy, which remains constant for a given element. We excited various metal elements at an energy of 10 keV and observed distinct characteristic peaks corresponding to each metal element at energies of 5.888 keV (Mn), 6.391 keV (Fe), 6.915 keV (Co), 7.461 keV (Ni), 8.028 keV (Cu), and 8.616 keV (Zn), respectively (Figure 2e). This observation demonstrated the effective and distinguishable X-ray signals generated by different Click-XRNs. Furthermore, the release behavior of metal ions from Click-XRNs was investigated, which indicated that almost all Click-XRNs exhibited a release of less than 10% within a 3 h period in aqueous solution (Figure S2b). The release of metal ions within the initial 3 h period may be attributed to weak electrostatic interactions between adsorbed metal ions and Click-XRNs.³⁰

Cell Labeling and Click-XRM

After successfully synthesizing different X-ray imaging probes using click chemistry, we subsequently evaluated the utility of this clickable labeling system for cell imaging. Mitochondria, which are double-layered membrane-coated organelles found in the majority of cells, serve as the primary sites for cellular energy production and aerobic respiration. Their diameter ranges from approximately 0.5 to 1.0 μm .³¹ We utilized 2 mL of ammonia to synthesize PDA NPs with an average particle size of 111.6 nm as the core. The nanoparticles were modified with azide groups and chelated Co^{2+} to prepare the Click-XRN_{Co} with an average particle size of 119.9 nm, which had enough localization accuracy for micrometer-sized mitochondria. As a mitochondria-targeting agent, TPP has demonstrated the capacity to effectively integrate diverse functional molecules and produce delocalized positive charges, affording it the capability to traverse the hydrophobic double-layer membrane of mitochondria.^{32–35} At present, as lipophilic cations, TPP has been widely used in the development of fluorogenic probes for detecting mitochondrial biomarkers, demonstrating its efficacy in specifically targeting mitochondria.^{32,36,37}

We selected HeLa cells and incubated them with TPP-PEG-alkyne to achieve modification of the mitochondria through alkyne groups. Subsequently, Click-XRN_{Co} was employed for the recognition and labeling of mitochondria (Figure 3a). The principle of Click-XRN_{Co} in recognizing and labeling is based on the copper(I)-catalyzed alkyne–azide cycloaddition (CuAAC) reaction, which occurs between the azide group on Click-XRN_{Co} and the modified alkyne group on

mitochondria. Soft X-rays in the “water-window” range, where water exhibits relatively high transparency to X-rays, while elements such as carbon, nitrogen and oxygen still interact with X-rays, are frequently employed for biological imaging.^{11,38,39} Here, we utilized soft X-rays with a wavelength of 2.36 nm and an energy of 525 eV to image HeLa cells, with the absorption of X-rays by the abundant C and N elements in the probe, providing imaging contrast. The resulting images showed typical mitochondrial morphology with high contrast (dark areas) (Figure 3b). Here, although the mitochondrial regions in the unlabeled HeLa cells could also generate imaging contrast at this energy (Figure 3c), the mitochondria labeled by the probe demonstrated significantly stronger imaging contrast compared to those without labeling (Figure 3d), allowing us to specifically track the biological target of interest under XRM using this clickable labeling system.

To demonstrate the ability of controllable preparation of appropriately sized Click-XRNs for labeling and imaging biological targets with varying scales, we selected smaller cell membranes as the biological targets. Cell membranes are specialized structures that surround the cell and its internal environments, consisting of a bilayer of phospholipids along with various other lipids, proteins, and carbohydrates. Its thickness measures 8–10 nm.⁴⁰ Click-XRN_{Co} was synthesized by modifying azide groups on the surface of sPDA NPs (with an average particle size of 3.7 nm) and chelating Co^{2+} , resulting in an average particle size of 3.9 nm, which was then used for cell membrane labeling. The glycoprotein labeling reagent Ac₄ManNAI is commonly used in alkyne modification. Upon hydrolysis by nonspecific esterases, the ester groups in Ac₄ManNAI release free sugar molecules that enter the sialic acid biosynthetic pathway. This enables the metabolic incorporation of the alkyne tag into membrane sialylated glycoconjugates for subsequent labeling via CuAAC.⁴¹ Here, we employed Ac₄ManNAI to modify alkynyl groups on the cell membrane of HeLa cells, enabling subsequent recognition and labeling using Click-XRN_{Co} (Figure 3e). Next, we used soft X-ray imaging (energy 525 eV, wavelength 2.36 nm) to visualize HeLa cells. However, the images (Figure S4) did not reveal a distinct cellular membrane structure. With the increase in the incident X-ray energy, the absorption coefficient of metal elements generally decreases. However, when reaching a certain photon energy threshold, there is a stepped increase in the absorption coefficient, enabling differentiation of metal elements based on variations in absorption intensity.^{42,43} In near-edge X-ray-absorption fine-structure (NEXAFS) spectrum, cobalt (Co) exhibits characteristic absorption peaks at 794 and 779 eV.⁴⁴ Therefore, we employed soft X-ray imaging with a photon energy of 780 eV to visualize the cellular samples. The resulting images exhibited high contrast (dark regions) that clearly delineate the membrane profile (Figure 3f). The optimal resolution of our Click-XRM system was ~ 30 nm, determined with the imaging of a star test pattern shown in Figure 3h. Line profiles of the cell membrane outlines indicate that their representative full width at half-maximum (fwhm) was about 41–52 nm (Figure 3g), suggesting the nanoscale spatial resolution of our labeling system.

Specifically, strain-promoted azide–alkyne cycloaddition (SPAAC), a type of click reaction, is a biological orthogonal reaction that refers to a category of chemical reactions that take place within living organisms without interfering with their endogenous biochemical processes.⁴⁵ Therefore, we systematically evaluated the cytotoxicity of the two PDA NPs, with

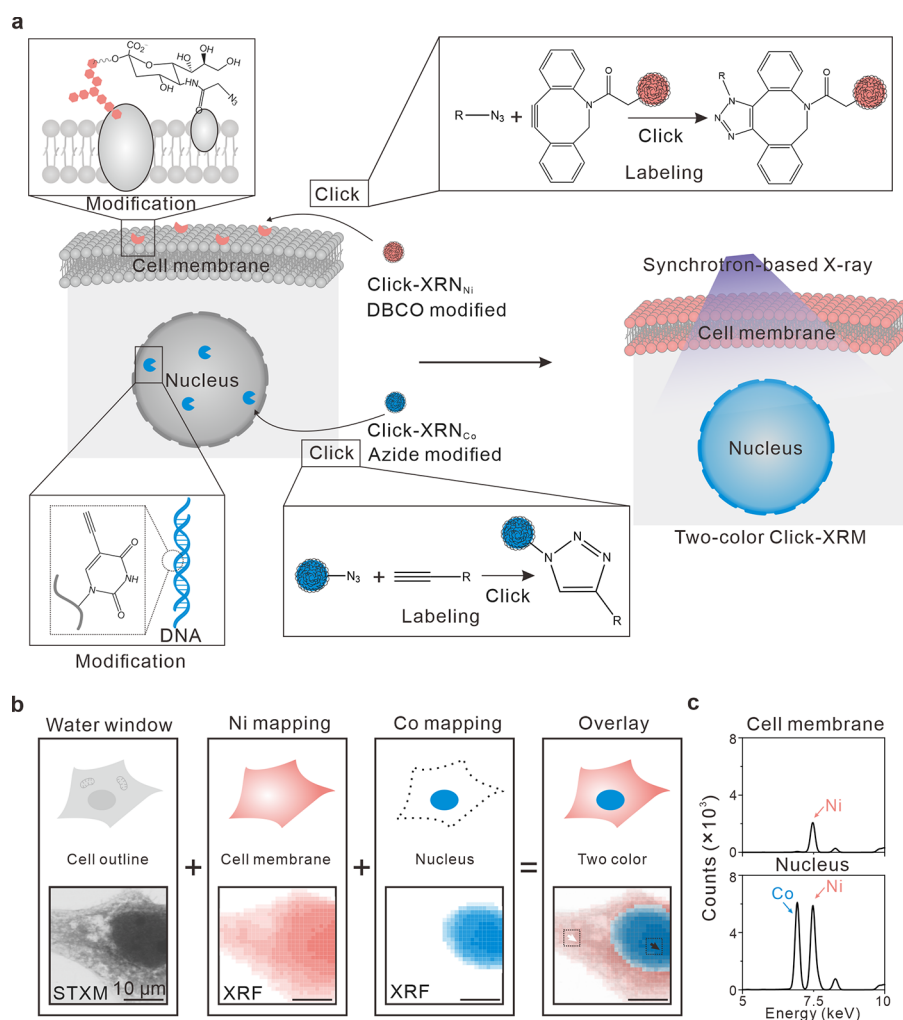


Figure 4. Two-color Click-XRM. (a) Schematic diagram of two-color Click-XRM. EdU and Ac₄ManNAz were incubated with HeLa cells to modify alkylnyl groups on DNA and azide groups on glycoproteins. Then the cell membrane and nucleus were labeled by Click-XRN_{Ni} (DBCO-modified) and Click-XRN_{Co} (azide-modified) in turn. Finally, the labeled cells were imaged using different synchrotron-based X-ray imaging methods. (b) Schematic showing (upper) and experimental (lower) of two-color Click-XRM for visualization of the cell membrane and nucleus. The labeled cells were imaged using STXM at a photon energy of 525 eV to show the cell outlines (first column), as well as obtaining XRF mapping images of Co and Ni elements excited at an energy of 10 keV (second and third column). The image (lower) in the fourth column was obtained by overlaying the images (lower) from the first three columns. The XRF full spectra were collected from the locations indicated by black and white arrows, corresponding to the position of the nucleus and cell membrane (fourth column), respectively. (c) The XRF full spectra of the HeLa cell nucleus and cell membrane. Arrows indicated the characteristic peaks of Co and Ni elements.

particle sizes of 111.6 and 3.7 nm, along with different Click-XRNs synthesized using these nanoparticles as the core. Within the experimental concentration range, both types of PDA NPs and Click-XRNs exhibited no apparent cytotoxic effects on HeLa cells (Figure S5), which was consistent with previous reports.^{29,30,46} All data suggest that Click-XRNs have laid a foundation for future applications in tracking cellular life activities.

Multicolor Click-XRM

Finally, we employed diverse metals and click reactions (Figure 4a) to achieve multicolor Click-XRM. Due to the excellent energy resolution of synchrotron-based X-rays, we introduced various metal elements with distinct XRF peaks into the click-XRM labeling system. sPDA NPs were used to separately chelate Co²⁺ and Ni²⁺ ions for synthesizing Click-XRN_{Co} and Click-XRN_{Ni}. At a photon energy of 10 keV, both Co and Ni elements can be excited, resulting in the emission of distinct secondary characteristic X-rays with energies of 6.915 and

7.461 keV, respectively, enabling the visualization of two distinguishable “colors” under XRM. To label two specific cellular targets, we utilized two click reactions: SPAAC and CuAAC. First, we chemically modified DBCO and azide groups on sPDA NPs, respectively. Subsequently, we chose cell nucleus and cell membranes as biological targets and modified alkylnyl and azide groups on the DNA (primarily located in the cell nucleus) and glycans (mainly distributed on the outer surface of the cell membrane) of HeLa cells, respectively. The modification of alkylnyl groups on DNA was achieved by incubating cells with EdU, a thymine nucleoside analogue that could substitute for thymine in the replicating DNA molecule during cell proliferation. The modification of azide groups on glycoprotein was achieved by incubating cells with Ac₄ManNAz, which was similar to the labeling of Ac₄ManNAI.^{47,48} Considering that the nuclear pore complex has a diameter of tens of nanometers,⁴⁹ it is difficult for Click-XRNs with a size exceeding 100 nm to enter the nucleus.

Therefore, we opted for sPDA NPs with an average particle size of 3.7 nm as the core for the preparation of multicolor Click-XRNs.

In subsequent experiments, EdU and Ac₄ManNAz were incubated with cells to modify the alkynyl groups on DNA and azide groups on glycoproteins. For the first round of labeling, Click-XRN_{Ni} (DBCO-modified) was introduced into the culture medium to label the cell membrane. Subsequently, Click-XRN_{Co} (azide-modified) was introduced into the culture medium to label the nucleus with Cu (I) as the catalyst for the second round of labeling (Figure 4a). The labeled cells were imaged using scanning transmission X-ray microscopy (STXM) at a photon energy of 525 eV (wavelength 2.36 nm), which showed the morphology of cells (Figure 4b, first column). Next, cells were imaged using synchrotron-based XRF at a photon energy of 10 keV. At this energy, both Co and Ni elements were excited, allowing us to obtain mapping images depicting the distribution of these two elements (Figure 4b, second and third columns). The resulting images showed localization of the cell membrane (Ni) and nucleus (Co), which can be attributed to the metal elements in Click-XRN_{Ni} and Click-XRN_{Co}. We conducted XRF spectroscopy analysis of the cell nucleus and cell membrane regions (Figure 4c). It could be observed that the XRF full spectrum of the cell membrane region exhibited a significant signal peak at 7.461 keV (Ni), indicating that the signal on it originated from the Ni element in probes. Here, due to the X-ray penetrating the entire cell and exciting the Ni element on the cell membrane, the mapping of the Ni element distribution covered the entire cell (Figure 4b, second column). We found that the XRF full spectrum of the cell nucleus showed evident signal peaks at 6.915 keV (Co) and 7.461 keV (Ni). During the imaging process, the X-rays penetrated the entire cell, causing the region of the cell nucleus to exhibit signals not only from Click-XRN_{Co}, but also from Click-XRN_{Ni} on the cell membrane. Finally, through the overlay of Co and Ni element mapping images with the cell morphology images under STXM, we generated a two-color image (Figure 4b, fourth column) that enables clear differentiation between the cell membrane and the nucleus. These results suggest the potential of this clickable labeling system for multiplexed XRM imaging.

DISCUSSION AND CONCLUSIONS

In conclusion, we reported a clickable intracellular biomolecular imaging probe (Click-XRN) suitable for XRM, which consists of an X-ray-sensitive signal module and a morphology module with a controllable particle size. The high efficiency, stability, and specificity of the click reaction ensured specific and effective labeling of the probe. Through using this labeling system, we obtained the image of diverse molecules and structures within the cells. We optimized the particle size and X-ray imaging energy of Click-XRM for diverse biological targets on different scales. In particular, the probe exhibited convenient chelation with various metal elements, and when combined with the exceptional elemental resolution of synchrotron-based X-rays, it effectively avoided crosstalk between tag signals. Based on this, we showed multicolor imaging of cells using XRM, thereby providing a powerful tool for elucidating cellular processes. Simultaneously, owing to the ability to modify alkynyl and sulfhydryl groups on the surface of PDA NPs, combined with the diversity of click reactions and catalytic systems, it holds promising potential for future development in preparing more Click-XRNs.⁵⁰

Compared to the existing synchrotron-based X-ray labeling system, clickable labeling system exhibits several advantages: (1) The X-ray imaging signal in the genetically tagging system is generated through the formation of DAB polymer, while achieving localization accuracy below 20 nm remains challenging due to the label diffusion within cells. Clickable labeling system is based on PDA NPs with controllable particle size and uniform morphology, enabling the attainment of nanometer-scale particles, thereby ensuring enhanced labeling precision. (2) Currently, the realization of living cell imaging using existing synchrotron-based X-ray probes remains challenging. By using biological orthogonal reactions such as SPAAC and combining them with the freezing platform, we are expected to achieve living cell imaging through Click-XRNs. Furthermore, compared with fluorescence microscopy, X-ray imaging boasts superior penetration and higher resolution. It eliminates issues like photobleaching, allowing for repeatable imaging of samples.⁵¹ This capability makes high-resolution imaging of intact cells or tissues achievable. Due to the rapid advancement of synchrotron-based XRM, researchers have currently achieved 3D imaging with a spatial resolution of less than 10 nm on transmission X-ray microscopy (TXM), which is in close proximity to the commonly utilized 4 nm resolution in electron microscope.⁸ Consequently, these cutting-edge technologies are expected to be employed for cell imaging in the future, enabling a more comprehensive understanding of the intricate cellular activities. Furthermore, through the modification of essential click reaction groups on neurons and glial cells within the brain, in conjunction with Click-XRNs and tissue transparency technology, there is an anticipation to visualize these elements using XRM, thereby offering a robust tool for synchrotron-based X-ray brain imaging.

METHODS

Synthesis of PDA NPs

To synthesize PDA NPs with a size of 111.6 nm, an ethanol solution (20 mL) and Milli-Q water (45 mL) were gently stirred at room temperature for 30 min after mixing with an ammonia aqueous solution (NH₃·H₂O, 2 mL, 28–30%). Dopamine hydrochloride (250 mg) was dissolved in Milli-Q water (5 mL), followed by injection into the above mixture solution. The reaction proceeded for 24 h before obtaining the PDA NPs through centrifugation and subsequent washing with water three times. By adjusting the amount of ammonia aqueous solution used, control over the size of PDA NPs was achieved (0.4, 0.6, 1, 1.5, or 2 mL for sizes of 841.7, 374.6, 244.9, 154.7, or 111.6 nm, respectively).

Synthesis of sPDA NPs

PDA NPs (111.6 nm, 20 mg) were first dissolved in NaOH aqueous solution (10 mL, 0.1 M) with vigorous stirring. After complete dissolution, an HCl aqueous solution (0.1 M) was added to the resulting solution for pH adjustment to 7.0 under sonication at an output power of 600 W for a duration of 3 min. The particles were then separated through centrifugation with a centrifugal filter (centrifugal filter device, MWCO = 30 kDa) at 8000 rpm for 10 min and were subsequently washed three times with Milli-Q water to remove the byproduct NaCl.

Surface Modification of PDA NPs

Ammonia aqueous solution (NH₃·H₂O, 28–30%) was added to the PDA NPs aqueous solution (1 mg/mL, 5 mL) to adjust the pH of the solution to 9. NH₂-PEG₂₀₀₀-N₃ or NH₂-

PEG₂₀₀₀-DBCO was then added to the mixed solution and reacted for 12 h to obtain PDA-N₃ or PDA-DBCO respectively.

Synthesis of Click-XRNs

Adjust the pH of the PDA-N₃ or PDA-DBCO aqueous solution to 5.5 by HCl aqueous solution (0.1 M). MnCl₂, FeSO₄, CoCl₂, NiCl₂, CuSO₄ and ZnCl₂ were added to the above solution and reacted at 40 °C for 3 h. Different Click-XRNs were retrieved by centrifugation at 10 000 rpm for 10 min and were then washed with Milli-Q water three times.

Preparation of Click-XRM Samples

For single-color click labeling, 12 h after seeding, cells were incubated with Ac₄ManNAI (final concentration 100 μM) or TPP-PEG-alkyne (100 μM) for 2 days. After 4% paraformaldehyde (PFA) fixation, each well of cells were incubated with 1 mL of CuAAC solution mixed with Click-XRN_{Co} (500 μg/mL), CuSO₄ (50 μM), THPTA (50 μM), and (+)-sodium-L-ascorbate (50 μM) in Milli-Q water for 30 min at 37 °C.

For two-color click labeling, 12 h after seeding, cells were incubated with Ac₄ManNAz (final concentration 100 μM) and EdU (100 μM) for 2 days. After 4% paraformaldehyde (PFA) fixation, each well of cells were incubated with 1 mL of SPAAC solution including Click-XRN_{Ni} (DBCO-modified) (500 μg/mL) in Milli-Q water for 30 min at 37 °C in the first round of labeling. After being washed three times by PBS, cells were incubated with 1 mL of CuAAC solution mixed by Click-XRN_{Co} (azide-modified) (500 μg/mL), CuSO₄ (50 μM), THPTA (50 μM), and (+)-sodium-L-ascorbate (50 μM) in Milli-Q water for 30 min at 37 °C in the second round of labeling. The two rounds of labeling exhibit excellent anticrossstalk ability due to utilizing distinct catalytic systems. Finally, cells were fixed with 4% PFA and then dehydrated in a graded gradient ethanol series.

Synchrotron-Based XRM and XRF Imaging

The X-ray microscopy images were acquired by STXM/transmission X-ray microscopy (TXM). STXM measurements were achieved at the BL08U1-A Soft X-ray Spectro Microscopy Beamline of the Shanghai Synchrotron Radiation Facility (SSRF). The monochromatic X-ray beam came out from a undulator and finally focused to a 30 nm spot on the sample via a 25 nm outermost-zone zone plate. The STXM imaging system was installed in an ~10⁻⁶ Torr vacuum chamber. The samples on a transparent Si₃N₄ film were actuated by a piezoelectric stage, scanned point-by-point by a focused spot, and resulted in a complete image. Images were recorded at the energy 525 eV, before the K-edge of O. STXM measurements were achieved at the BL07W Soft X-ray Microscopy beamline of the National Synchrotron Radiation Laboratory (NSRL). The samples on a transparent Si₃N₄ film were recorded by a CCD detector as a series of images and assembled into a mosaic. Images were recorded at energy levels of 525 and 780 eV.

The X-ray fluorescence mapping images were obtained by XRF. XRF measurements were performed at the BL15U1 The Hard X-ray Microfocusing Beamline of the SSRF. The exciting light X-ray beam is generated by a vacuum hybrid undulator and focused to a 2-μm spot on the sample at 10 keV. The emitting light X-ray fluorescence from each site of sample were detected by a CCD detector sequentially. Images were recorded within the energy region of Mn (between 5.75 and 6.05 keV), Fe (between 6.25 and 6.55 keV), Co (between 6.78

and 7.08 keV), Ni (between 7.33 and 7.63 keV), Cu (between 7.89 and 8.19 keV), and Zn (between 8.49 and 8.79 keV).

ASSOCIATED CONTENT

Supporting Information

The Supporting Information is available free of charge at <https://pubs.acs.org/doi/10.1021/jacsau.4c00056>.

Supplementary experimental details, ICP-MS analysis, TEM-EDS images, cell viability assessments, and X-ray images of cells in the control groups (PDF)

AUTHOR INFORMATION

Corresponding Authors

Jun Hu – Institute of Materiobiology, College of Science, Shanghai University, Shanghai 200444, China; Division of Physical Biology, CAS Key Laboratory of Interfacial Physics and Technology, Shanghai Institute of Applied Physics, Chinese Academy of Sciences, University of Chinese Academy of Sciences, Shanghai 201800, China; Email: hujun64@shu.edu.cn

Xiaoqing Cai – Shanghai Synchrotron Radiation Facility (SSRF), Shanghai Advanced Research Institute, Chinese Academy of Sciences, Shanghai 201204, China; Email: Caixq@sari.ac.cn

Ying Zhu – Institute of Materiobiology, College of Science, Shanghai University, Shanghai 200444, China; Division of Physical Biology, CAS Key Laboratory of Interfacial Physics and Technology, Shanghai Institute of Applied Physics, Chinese Academy of Sciences, University of Chinese Academy of Sciences, Shanghai 201800, China; orcid.org/0000-0003-0418-919X; Email: zhuying331@shu.edu.cn

Authors

Qiaowei Tang – Institute of Materiobiology, College of Science, Shanghai University, Shanghai 200444, China; Xiangfu Laboratory, Jiashan 314102, China

Dapeng Yin – Division of Physical Biology, CAS Key Laboratory of Interfacial Physics and Technology, Shanghai Institute of Applied Physics, Chinese Academy of Sciences, University of Chinese Academy of Sciences, Shanghai 201800, China

Yubo Liu – Division of Physical Biology, CAS Key Laboratory of Interfacial Physics and Technology, Shanghai Institute of Applied Physics, Chinese Academy of Sciences, University of Chinese Academy of Sciences, Shanghai 201800, China

Jichao Zhang – Shanghai Synchrotron Radiation Facility (SSRF), Shanghai Advanced Research Institute, Chinese Academy of Sciences, Shanghai 201204, China

Yong Guan – National Synchrotron Radiation Laboratory, University of Science and Technology of China, Hefei 230029, China; orcid.org/0000-0002-7596-3114

Huatiang Kong – Shanghai Synchrotron Radiation Facility (SSRF), Shanghai Advanced Research Institute, Chinese Academy of Sciences, Shanghai 201204, China

Yiliu Wang – Division of Physical Biology, CAS Key Laboratory of Interfacial Physics and Technology, Shanghai Institute of Applied Physics, Chinese Academy of Sciences, University of Chinese Academy of Sciences, Shanghai 201800, China

Xiangzhi Zhang – Shanghai Synchrotron Radiation Facility (SSRF), Shanghai Advanced Research Institute, Chinese Academy of Sciences, Shanghai 201204, China

Jiang Li – Institute of Materiobiology, College of Science, Shanghai University, Shanghai 200444, China; Division of Physical Biology, CAS Key Laboratory of Interfacial Physics and Technology, Shanghai Institute of Applied Physics, Chinese Academy of Sciences, University of Chinese Academy of Sciences, Shanghai 201800, China

Lihua Wang – Institute of Materiobiology, College of Science, Shanghai University, Shanghai 200444, China; Division of Physical Biology, CAS Key Laboratory of Interfacial Physics and Technology, Shanghai Institute of Applied Physics, Chinese Academy of Sciences, University of Chinese Academy of Sciences, Shanghai 201800, China

Complete contact information is available at:

<https://pubs.acs.org/10.1021/jacsau.4c00056>

Author Contributions

[‡]Q.T., D.Y. and Y.L. contributed equally. CRediT: **Ying Zhu** supervised the research. **Qiaowei Tang, Dapeng Yin** and **Yubo Liu** performed the experiments. **Jichao Zhang, Yong Guan** and **Xiangzhi Zhang** helped in guidance of X-ray microscopy. **Huating Kong** and **Yiliu Wang** aided in cell experiments. **Jiang Li** and **Lihua Wang** performed critical revisions. **Ying Zhu, Jun Hu** and **Xiaoqing Cai** analyzed the data and wrote versions of manuscript. All authors discussed and commented on the manuscript.

Notes

The authors declare no competing financial interest.

ACKNOWLEDGMENTS

We thank the staff of BL15U1 hard X-ray micro-focusing beamline and the BL08U1A soft X-ray spectromicroscopy beamline of Shanghai Synchrotron Radiation Facility (SSRF, China), and BL07W soft X-ray imaging beamline of the National Synchrotron Radiation Laboratory (NSRL, China) for their technical support and assistance. This work was supported by the National Key R&D Program of China (2023YFC3404200), the National Natural Science Foundation of China (22022410, 82050005, and 22393934), 2022 Shanghai “Science and Technology Innovation Action Plan” Fundamental Research Project (22JC1401203), and the Science Foundation of the Shanghai Municipal Science and Technology Commission (21dz2210100).

REFERENCES

- (1) Liu, T.-L.; Upadhyayula, S.; Milkie, D. E.; Singh, V.; Wang, K.; Swinburne, I. A.; Mosaliganti, K. R.; Collins, Z. M.; Hiscock, T. W.; Shea, J.; et al. Observing the cell in its native state: Imaging subcellular dynamics in multicellular organisms. *Science* **2018**, *360*, No. eaaq1392.
- (2) Laporte, M. H.; Klena, N.; Hamel, V.; Guichard, P. Visualizing the native cellular organization by coupling cryofixation with expansion microscopy (Cryo-ExM). *Nat. Methods* **2022**, *19*, 216–222.
- (3) Miao, J.; Ishikawa, T.; Robinson, I. K.; Murnane, M. M. Beyond crystallography: Diffractive imaging using coherent X-ray light sources. *Science* **2015**, *348*, 530–535.
- (4) Shahsavari, A.; Stohler, P.; Bourenkov, G.; Zimmermann, I.; Siegrist, M.; Guba, W.; Pinard, E.; Sinning, S.; Seeger, M. A.; Schneider, T. R.; et al. Structural insights into the inhibition of glycine reuptake. *Nature* **2021**, *591*, 677–681.
- (5) Guttman, P.; Bittencourt, C.; Rehbein, S.; Umek, P.; Ke, X.; Van Tendeloo, G.; Ewels, C. P.; Schneider, G. Nanoscale spectroscopy with polarized X-rays by NEXAFS-TXM. *Nat. Photonics* **2012**, *6*, 25–29.
- (6) Okolo, C. A.; Kounatidis, I.; Groen, J.; Nahas, K. L.; Balint, S.; Fish, T. M.; Koronfel, M. A.; Cortajarena, A. L.; Dobbie, I. M.; Pereiro, E.; et al. Sample preparation strategies for efficient correlation of 3D SIM and soft X-ray tomography data at cryogenic temperatures. *Nat. Protoc.* **2021**, *16*, 2851–2885.
- (7) Schneider, G.; Guttman, P.; Heim, S.; Rehbein, S.; Mueller, F.; Nagashima, K.; Heymann, J. B.; Müller, W. G.; McNally, J. G. Three-dimensional cellular ultrastructure resolved by X-ray microscopy. *Nat. Methods* **2010**, *7*, 985–987.
- (8) De Andrade, V.; Nikitin, V.; Wojcik, M.; Deriy, A.; Bean, S.; Shu, D.; Mooney, T.; Peterson, K.; Kc, P.; Li, K.; et al. Fast X-ray nanotomography with sub-10 nm resolution as a powerful imaging tool for nanotechnology and energy storage applications. *Adv. Mater.* **2021**, *33*, 2008653.
- (9) Thibault, P.; Dierolf, M.; Menzel, A.; Bunk, O.; David, C.; Pfeiffer, F. High-resolution scanning X-ray diffraction microscopy. *Science* **2008**, *321*, 379–382.
- (10) Dierolf, M.; Menzel, A.; Thibault, P.; Schneider, P.; Kewish, C. M.; Wepf, R.; Bunk, O.; Pfeiffer, F. Ptychographic X-ray computed tomography at the nanoscale. *Nature* **2010**, *467*, 436–439.
- (11) Chao, W.; Harteneck, B. D.; Liddle, J. A.; Anderson, E. H.; Attwood, D. T. Soft X-ray microscopy at a spatial resolution better than 15 nm. *Nature* **2005**, *435*, 1210–1213.
- (12) Zhang, M.; Guan, Y.; Dang, Z.; Zhang, P.; Zheng, Z.; Chen, L.; Kuang, W.; Wang, C.; Liang, G. Directly observing intracellular nanoparticle formation with nanocomputed tomography. *Sci. Adv.* **2020**, *6*, No. eaba3190.
- (13) White, K. L.; Singla, J.; Loconte, V.; Chen, J.-H.; Ekman, A.; Sun, L.; Zhang, X.; Francis, J. P.; Li, A.; Lin, W.; et al. Visualizing subcellular rearrangements in intact β cells using soft X-ray tomography. *Sci. Adv.* **2020**, *6*, No. eabc8262.
- (14) Ice, G. E.; Budai, J. D.; Pang, J. W. L. The race to X-ray microbeam and nanobeam science. *Science* **2011**, *334*, 1234–1239.
- (15) Adair, K. R.; Banis, M. N.; Zhao, Y.; Bond, T.; Li, R.; Sun, X. Temperature-dependent chemical and physical microstructure of Li metal anodes revealed through synchrotron-based imaging techniques. *Adv. Mater.* **2020**, *32*, 2002550.
- (16) Gao, J.; Gu, Z. Toward nanoscopic cellular imaging by X-ray. *Natl. Sci. Rev.* **2021**, *8*, nwaa206.
- (17) Zhu, Y.; Zhang, J.; Li, A.; Zhang, Y.; Fan, C. Synchrotron-based X-ray microscopy for sub-100nm resolution cell imaging. *Curr. Opin. Chem. Biol.* **2017**, *39*, 11–16.
- (18) Lai, H. M.; Tang, Y.; Lau, Z. Y. H.; Campbell, R. A. A.; Yau, J. C. N.; Chan, C. C. Y.; Chan, D. C. W.; Wong, T. Y.; Wong, H. K. T.; Yan, L. Y. C.; et al. Antibody stabilization for thermally accelerated deep immunostaining. *Nat. Methods* **2022**, *19*, 1137–1146.
- (19) Zhang, C.; Yao, S.; Xu, C.; Chang, Y.; Zong, Y.; Zhang, K.; Zhang, X.; Zhang, L.; Chen, C.; Zhao, Y.; et al. 3D imaging and quantification of the integrin at a single-cell base on a multisignal nanoprobe and synchrotron radiation soft X-ray tomography microscopy. *Anal. Chem.* **2021**, *93*, 1237–1241.
- (20) Li, T.; He, B.; Zhang, X.; Fan, J.; Gao, L.; Sun, Z.; Zhang, J.; Guo, A.; Pan, D.; Yin, X.; et al. Three-dimensional quantitative coherent diffraction imaging of staphylococcus aureus treated with peptide-mineralized Au-cluster probes. *Anal. Chem.* **2022**, *94*, 13136–13144.
- (21) Zhang, C.; Zhang, K.; Cui, Y.; Guo, Y.; Wang, C.; Xu, C.; Yao, Q.; Zhao, Y.; Chen, C.; Wang, Y. Multifunctional nanoprobe for 3d nanoresolution imaging of intact cell HER2 protein with hard x-ray tomography. *Anal. Chem.* **2023**, *95*, 2129–2133.
- (22) Yan, M.; Zuo, T.; Zhang, J.; Wang, Y.; Zhu, Y.; Wang, L.; Zhou, Y.; Sun, Y. A bimodal probe for fluorescence and synchrotron X-ray fluorescence imaging of dopaminergic neurons in the brain. *Chem. Commun.* **2022**, *58*, 713–715.
- (23) Kong, H.; Zhang, J.; Li, J.; Wang, J.; Shin, H.-J.; Tai, R.; Yan, Q.; Xia, K.; Hu, J.; Wang, L.; et al. Genetically encoded X-ray cellular imaging for nanoscale protein localization. *Natl. Sci. Rev.* **2020**, *7*, 1218–1227.

- (24) Kolb, H. C.; Finn, M. G.; Sharpless, K. B. Click chemistry: Diverse chemical function from a few good reactions. *Angew. Chem., Int. Ed.* **2001**, *40*, 2004–2021.
- (25) Kolb, H. C.; Sharpless, K. B. The growing impact of click chemistry on drug discovery. *Drug Discovery Today* **2003**, *8*, 1128–1137.
- (26) Devaraj, N. K.; Finn, M. G. Introduction: Click chemistry. *Chem. Rev.* **2021**, *121*, 6697–6698.
- (27) Yoon, H. Y.; Lee, D.; Lim, D.-K.; Koo, H.; Kim, K. Copper-free click chemistry: Applications in drug delivery, cell tracking, and tissue engineering. *Adv. Mater.* **2022**, *34*, 2107192.
- (28) Agrahari, A. K.; Bose, P.; Jaiswal, M. K.; Rajkhowa, S.; Singh, A. S.; Hotha, S.; Mishra, N.; Tiwari, V. K. Cu(I)-catalyzed click chemistry in glycoscience and their diverse applications. *Chem. Rev.* **2021**, *121*, 7638–7956.
- (29) Miao, Z.-H.; Wang, H.; Yang, H.; Li, Z.-L.; Zhen, L.; Xu, C.-Y. Intrinsically Mn²⁺-chelated polydopamine nanoparticles for simultaneous magnetic resonance imaging and photothermal ablation of cancer cells. *ACS Appl. Mater. Interfaces* **2015**, *7*, 16946–16952.
- (30) Fan, Q.; Cheng, K.; Hu, X.; Ma, X.; Zhang, R.; Yang, M.; Lu, X.; Xing, L.; Huang, W.; Gambhir, S. S.; et al. Transferring biomarker into molecular probe: Melanin nanoparticle as a naturally active platform for multimodality imaging. *J. Am. Chem. Soc.* **2014**, *136*, 15185–15194.
- (31) Monzel, A. S.; Enríquez, J. A.; Picard, M. Multifaceted mitochondria: moving mitochondrial science beyond function and dysfunction. *Nat. Metab.* **2023**, *5*, 546–562.
- (32) Liu, K.; Zhang, Z.; Liu, R.; Li, J. P.; Jiang, D.; Pan, R. Click-chemistry-enabled nanopipettes for the capture and dynamic analysis of a single mitochondrion inside one living cell. *Angew. Chem., Int. Ed.* **2023**, *62*, No. e202303053.
- (33) Ni, F.; Zhu, Z.; Tong, X.; Zeng, W.; An, K.; Wei, D.; Gong, S.; Zhao, Q.; Zhou, X.; Yang, C. Hydrophilic, red-emitting, and thermally activated delayed fluorescence emitter for time-resolved luminescence imaging by mitochondrion-induced aggregation in living cells. *Adv. Sci.* **2019**, *6*, 1801729.
- (34) Zhang, X.; Wang, Y.; Wei, G.; Zhao, J.; Yang, G.; Zhou, S. Stepwise dual targeting and dual responsive polymer micelles for mitochondrion therapy. *J. Controlled Release* **2020**, *322*, 157–169.
- (35) Truong Hoang, Q.; Huynh, K. A.; Nguyen Cao, T. G.; Kang, J. H.; Dang, X. N.; Ravichandran, V.; Kang, H. C.; Lee, M.; Kim, J.-E.; Ko, Y. T.; et al. Piezocatalytic 2D WS₂ nanosheets for ultrasound-triggered and mitochondria-targeted piezodynamic cancer therapy synergized with energy metabolism-targeted chemotherapy. *Adv. Mater.* **2023**, *35*, 2300437.
- (36) Fu, G.; Yin, G.; Niu, T.; Wu, W.; Han, H.; Chen, H.; Yin, P. A novel ratiometric fluorescent probe for the detection of mitochondrial pH dynamics during cell damage. *Analyst* **2021**, *146*, 620–627.
- (37) Wang, B.; Wang, Y.; Wu, H.; Song, X.; Guo, X.; Zhang, D.; Ma, X.; Tan, M. A mitochondria-targeted fluorescent probe based on TPP-conjugated carbon dots for both one- and two-photon fluorescence cell imaging. *RSC Adv.* **2014**, *4*, 49960–49963.
- (38) Shabbir, B.; Liu, J.; Krishnamurthi, V.; Ayyubi, R. A. W.; Tran, K.; Tawfik, S. A.; Hossain, M. M.; Khan, H.; Wu, Y.; Shivananju, B. N.; et al. Soft X-ray detectors based on SnS nanosheets for the water window region. *Adv. Funct. Mater.* **2022**, *32*, 2105038.
- (39) Kounatidis, I.; Stanifer, M. L.; Phillips, M. A.; Paul-Gilloteaux, P.; Heiligenstein, X.; Wang, H.; Okolo, C. A.; Fish, T. M.; Spink, M. C.; Stuart, D. I.; et al. 3D correlative cryo-structured illumination fluorescence and soft X-ray microscopy elucidates reovirus intracellular release pathway. *Cell* **2020**, *182*, 515–530.e517.
- (40) Hou, W.; Ma, D.; He, X.; Han, W.; Ma, J.; Wang, H.; Xu, C.; Xie, R.; Fan, Q.; Ye, F.; et al. Subnanometer-precision measurements of transmembrane motions of biomolecules in plasma membranes using quenchers in extracellular environment. *Nano Lett.* **2021**, *21*, 485–491.
- (41) Altmann, S.; Mut, J.; Wolf, N.; Meißner-Weigl, J.; Rudert, M.; Jakob, F.; Gutmann, M.; Lühmann, T.; Seibel, J.; Ebert, R. Metabolic glycoengineering in hMSC-TERT as a model for skeletal precursors by using modified azide/alkyne monosaccharides. *Int. J. Mol. Sci.* **2021**, *22*, 2820.
- (42) Beaumont, S. K.; Alayoglu, S.; Specht, C.; Michalak, W. D.; Pushkarev, V. V.; Guo, J.; Kruse, N.; Somorjai, G. A. Combining in situ NEXAFS spectroscopy and CO₂ methanation kinetics to study Pt and Co nanoparticle catalysts reveals key insights into the role of platinum in promoted cobalt catalysis. *J. Am. Chem. Soc.* **2014**, *136*, 9898–9901.
- (43) Sivkov, D.; Petrova, O.; Mingaleva, A.; Ob'edkov, A.; Kaverin, B.; Gusev, S.; Vilkov, I.; Isaenko, S.; Bogachuk, D.; Skandakov, R.; et al. The structure and chemical composition of the Cr and Fe pyrolytic coatings on the MWCNTs' surface according to NEXAFS and XPS spectroscopy. *Nanomaterials* **2020**, *10*, 374.
- (44) An, K.; Alayoglu, S.; Musselwhite, N.; Plamthottam, S.; Melaet, G.; Lindeman, A. E.; Somorjai, G. A. Enhanced CO oxidation rates at the interface of mesoporous oxides and Pt nanoparticles. *J. Am. Chem. Soc.* **2013**, *135*, 16689–16696.
- (45) Yang, M.; Li, J.; Chen, P. R. Transition metal-mediated bioorthogonal protein chemistry in living cells. *Chem. Soc. Rev.* **2014**, *43*, 6511–6526.
- (46) Liu, Y.; Ai, K.; Lu, L. Polydopamine and its derivative materials: Synthesis and promising applications in energy, environmental, and biomedical fields. *Chem. Rev.* **2014**, *114*, 5057–5115.
- (47) Salic, A.; Mitchison, T. J. A chemical method for fast and sensitive detection of DNA synthesis in vivo. *Proc. Natl. Acad. Sci. U. S. A.* **2008**, *105*, 2415–2420.
- (48) Spicciarich, D. R.; Nolley, R.; Maund, S. L.; Purcell, S. C.; Herschel, J.; Iavarone, A. T.; Peehl, D. M.; Bertozzi, C. R. Bioorthogonal labeling of human prostate cancer tissue slice cultures for glycoproteomics. *Angew. Chem., Int. Ed.* **2017**, *56*, 8992–8997.
- (49) Zhu, X.; Huang, G.; Zeng, C.; Zhan, X.; Liang, K.; Xu, Q.; Zhao, Y.; Wang, P.; Wang, Q.; Zhou, Q.; et al. Structure of the cytoplasmic ring of the *Xenopus laevis* nuclear pore complex. *Science* **2022**, *376*, No. eabl8280.
- (50) Ryu, J. H.; Messersmith, P. B.; Lee, H. Polydopamine surface chemistry: A decade of discovery. *ACS Appl. Mater. Interfaces* **2018**, *10*, 7523–7540.
- (51) Strotton, M.; Hosogane, T.; di Michiel, M.; Moch, H.; Varga, Z.; Bodenmiller, B. Multielement Z-tag imaging by X-ray fluorescence microscopy for next-generation multiplex imaging. *Nat. Methods* **2023**, *20*, 1310–1322.